NASA-CR-200175

11-43-CR

004794

J-0020

Sea-Ice Feature Mapping using JERS-1 Imagery

James Maslanik and John Heinrichs

CB449, University of Colorado, Boulder, Colorado, 80309 USA
jimm@northwind.colorado.edu

Abstract JERS-1 SAR and OPS imagery are examined in combination with other data sets to investigate the utility of the JERS-1 sensors for mapping fine-scale sea ice conditions. Combining ERS-1 C band and JERS-1 L band SAR aids in discriminating multiyear and first-year ice. Analysis of OPS imagery for a field site in the Canadian Archipelago highlights the advantages of OPS's high spatial and spectral resolution for mapping ice structure, melt pond distribution, and surface albedo.

1. Introduction

Here, we consider the capabilities of JERS-1 synthetic aperture radar (SAR) and Optical Sensor System (OPS) imagery for detecting sea-ice features, mapping ice types, and determining surface albedo as a function of ice type. The discussion is divided into two sections. The first section describes the use of JERS-1 C-band SAR alone and in combination with ERS-1 L-band SAR for mapping first-year and multiyear ice in the Arctic Beaufort Sea. The second section discusses applications of OPS imagery to document ice type and melt conditions at a field site on shore-fast ice in the Canadian Archipelago.

1.1 Evaluating the JERS-1 SAR for Distinguishing Sea Ice Types - a Comparison With ERS-1 SAR Data

Because of their high spatial resolution and freedom from the effects of clouds and darkness, satellite-borne SAR instruments have been of great value for conducting studies of sea ice dynamics and growth. The advent of the L band SAR instrument aboard the JERS-1 spacecraft offers another exciting tool for sea ice research, both by itself and in combination with other microwave and electro-optical sensors. In the following section, we evaluate the potential of the JERS-1 SAR for discriminating between sea ice types - a problem which is vital for mapping sea ice and validating modern coupled ice/ocean models - by comparing the JERS-1 SAR ice signatures with those from the C-band SAR carried aboard the ERS-1 satellite. In addition, the advantages of combining data from both sensors to identify different ice types are illustrated and discussed.

1.1.1 Data Processing

A co-located pair of JERS-1 and ERS-1 SAR images, with a nominal spatial resolution of 12.5 m, was acquired on February 18, 1993 for an area in the Beaufort Sea centered at 76.3° N, 142.75° W. The time and position of the study area were chosen to depict typical pack ice during winter, when changes in the ice surface that can affect its appearance in SAR imagery are at a minimum. After acquisition, the images were converted from Digital Number (DN) values, calibrated using the operational ASF algorithm (Kwok and Cunningham 1993), and converted to backscatter values in dB (decibels). The two images were then coregistered by identifying the overlapping portions, selecting tie points, and applying a polynomial image warping procedure. The results of the calibration and coregistration are illustrated in Figures 1 and 2, which show a portion of the overlapping area of the ERS-1 and JERS-1 images, respectively.

MITI

NASDA
宇宙開発事業団

FINAL REPORT OF JERS-1/ERS-1 SYSTEM VERIFICATION PROGRAM

VOLUME II

March 1995

Ministry of International Trade and Industry
National Space Development Agency of Japan

1.1.2 General Observations

The primary difference in the appearance of sea ice at L band (1.2 GHz or 23.5 cm) and C band (5.3 GHz or 5.7 cm) is the reversal of the backscatter ordering of first-year (FY) and multiyear (MY) ice (Onstott 1992). (Multiyear ice is defined here as sea ice that has survived at least one melt season). At C band frequencies (Figure 1), MY ice has a high backscatter, and thus a bright appearance, due to the presence of a multitude of small bubbles in ice hummocks (Hallikainen and Winebrenner 1992). FY ice tends to have a lower backscatter. At the L band frequencies of the JERS-1 SAR (Figure 2), the opposite is true. The greater penetration depth of the lower-frequency radiation reduces backscatter from MY ice, while the coarser-scale, sharply-angled features (pressure ridges, rubble fields) typical of FY ice are more reflective than at C band (Onstott 1992). It has also been noted that the edges of ice floes are less distinct at L band frequencies, and this can be readily seen in Figure 2. The backscatter of young ice (nilas and grey ice) is dominated by the effects of brine content on the dielectric constant, and signatures are similar for both L and C bands.

1.1.3 Statistical Analysis

In order to quantify the relative signatures of FY and MY ice in JERS-1 SAR data, portions of the co-registered image pair that belonged to a specific ice type were identified and used in a statistical analysis. The images were enhanced by contrast stretching, and manual interpretation was used to select polygonal subsets of the ERS-1 image that were well-defined and homogenous. Since young ice types cannot be effectively distinguished in C band imagery (Steffen and Heinrichs 1994), the selection of representative areas was limited to MY ice and two FY types. The two FY types were designated FY I and FY II following Steffen and Heinrichs (1994). After selection of the polygonal training areas from the ERS-1 SAR imagery, the matching JERS-1 SAR data were extracted. Means and standard deviations were calculated for all three ice types as seen in both instruments (Table 1). From Table 1 and Figure 3, which graphically illustrate the results of the statistical analysis, several observations can be made. First, the backscatter order reversal described qualitatively above is borne out by the mean backscatter values - the JERS-1 SAR data show FY ice having a higher backscatter than MY ice in contrast to the results from the ERS-1 SAR. Second, the standard deviations of the ice types are slightly greater in the JERS-1 data. As mentioned above, ice floe boundaries are not as well defined at the lower L-band frequencies, and this is likely the cause of the greater variation seen in the JERS-1 statistics. Finally, while there is some overlap between FY and MY ice in the data from each SAR sensor, along the diagonal in Figure 3 the separation is much more obvious, suggesting that combining data from both instruments is more effective than interpreting data from either SAR individually.

1.1.4 Combining Data from Both Sensors

To fully evaluate the use of data from both the JERS-1 and ERS-1 SAR instruments, an independent source of "truth" would be required. Nevertheless, by image processing techniques the potential of a multispectral approach can be explored. Figure 4 shows a color composite image with JERS-1 SAR data displayed in red and ERS-1 data in green. In keeping with the results noted above, there is a clear difference between FY and MY ice, with the FY in red tones (since it is bright in the JERS-1 image) and the MY in green. Furthermore, young ice areas, which have similar signatures as seen by both sensors, have a yellowish color.

1.2 Summary of SAR Analysis for the Beaufort Ice Pack

Our study has confirmed earlier results from ground and aircraft-mounted L-band SAR instruments (Onstott 1992) showing a reversal in the backscatter ordering of FY and MY ice. In addition, the performance of the JERS-1 SAR for identifying ice types is shown to be roughly equivalent to the ERS-1 SAR, except for the inherently slightly poorer definition of ice floes in low-frequency radar imagery. Finally, using data from both instruments together offers a significantly improved capability over using each individually. A more detailed study, using high-resolution visible and IR imagery, is an obvious next step in developing this promising approach.

2.1 Sea Ice Feature Mapping using JERS-1 Optical Sensor System (OPS) Imagery

Monitoring of the ice cover using optical-wavelength imagery is typically done using moderate-resolution (approximately 1 km) data from sensors such as the Advanced Very High Resolution Radiometer (AVHRR). However, case studies using high-resolution imagery are necessary to verify the ice-type mapping described above, and to map melt pond coverage, albedo, and snowcover characteristics on individual ice floes. The JERS-1 visible and near-infrared radiometer (VNIR) offers higher spatial resolution (18 m) than Landsat Thematic Mapper (30 m) and higher spectral resolution than SPOT multispectral data (20 m). Thus, the VNIR provides some potentially unique capabilities for mapping small surface features on the ice pack. Here, we consider the qualities of imagery acquired for the location of the Seasonal Sea Ice Monitoring and Modeling Site (SIMMS) field camp near Resolute Bay in the Canadian Archipelago during the mid-summer melt period in 1992.

In the following discussion, AVHRR imagery provides a general view of conditions three weeks earlier than the VNIR image and prior to melt. The features apparent in the VNIR data are considered in this context, and then compared to an aircraft-acquired SAR image. (The JERS-1 SAR image available for this comparison was not usable due to transmission-pulse problems in the SAR during that portion of its life cycle). Specifically, we consider: 1) general conditions of a retreating and melting ice cover in Lancaster Sound; 2) characteristics of a multiyear ice floe as compared to the aircraft SAR and field observations; and 3) approximate narrow-band surface albedos over different ice types during peak melt.

2.1.1 Sea Ice Conditions

The JERS-1 VNIR image used was acquired on July 17, 1992 for a portion of the Canadian Archipelago centered near Cornwallis Island (Figures 5 and 6). Field data were collected in this area at camps established on first-year ice and multiyear ice during April 3 through June 27, 1992 (Reddan, 1992). As late as June 27, when the ice camps were removed, snow was abundant and in only the initial stages of melt, and breakup of the shore-fast ice in Lancaster Sound had not yet begun in earnest (e.g., Figure 5). As shown by the VNIR composite in Figure 6, conditions had changed dramatically by July 17. The high resolution of the VNIR channels reveals fine detail within the ice floes that have broken free from the fast ice (Figure 7). Land areas are snow-free except in drainages where drifted snow can reach several meters deep. The southern edge of the remaining arch of shore-fast ice in Wellington Channel (between Cornwallis and Devon Islands) corresponds to the location of a change in surface reflectivity in the AVHRR image in Figure 5, possibly related to differences in the formation histories of the ice in Wellington Channel and Lancaster Sound. For reference, the width of Wellington Channel at the fast ice edge is 39 km.

Within the remaining fast ice in Wellington Channel, variations in tone and texture in the VNIR image in Figure 6 are typical of the variability in the mixture of smooth and deformed first-year ice with interspersed multiyear ice floes. The large multiyear floe (6.4 km wide at the longest axis) indicated in Figure 6 and enlarged in Figure 8 was the site of the multiyear ice camp. The surface of the floe was typical of multiyear ice, with raised hummocks and depressions formed at the locations of melt ponds where surface water accumulates during melt. This multiyear floe was estimated in the field to be between 3 and 5 years old. Snow depths on the floe in May were between 40 to 100 cm in the melt pond locations and 10 to 25 cm on hummocks (Papakyriakou, 1992).

2.1.2 Melt Pond Coverage

By July 17, the VNIR data suggest that extensive melt was underway. Unfortunately, no direct field observations were available at this time, but melt pond formation by this date was likely, based on general conditions elsewhere in the region. The mottled pattern on the multiyear floe in Figure 8 is typical of that expected from melt ponds with standing water interspersed with hummocks. In contrast, melt on the smoother first-year ice adjacent to the floe and in the drifting floes in Lancaster Sound is typically distributed as shallower, more wide-spread melt ponds, which is consistent with the tones and textures shown in the VNIR image.

The actual fraction of ice floes that are covered by melt ponds on different ice types in the Arctic is not well known. Estimates range from about 20% to 40% of the ice surface covered by ponded meltwater in mid-summer (Barry 1989). To provide a rough estimate of meltpond fraction on the multiyear floe, a threshold channel 3 reflectance was chosen to map the apparent ponded areas, with a resulting melt pond coverage of 56% for a threshold DN of 60. Even at 18 m spatial resolution, some within-pixel mixing of pond and hummock area will occur, but the mapped spatial patterns and proportions of ponding are reasonable.

2.1.3 Floe Characteristics in Aircraft SAR and OPS VNIR Imagery

The combination of floe shape and surface features in the VNIR image is typical of multiyear ice floes. However, the contrast between first-year ice and the multiyear floe is much greater in the aircraft SAR image (Figure 9). This 15 m resolution, X band (3 cm wavelength) SAR image was acquired by a STAR-2 aircraft SAR system on board an Intera Technologies Ltd. Challenger under contract to the Canadian AES Ice Centre. As noted above regarding the comparison of JERS-1 L band and ERS-1 C band SAR, backscatter in the short-wavelength X band STAR-2 image is considerably higher from the multiyear floe than from the first-year ice during dry-snow conditions. Once melt starts, such distinctions are typically lost in the SAR signal (Winebrenner et al., 1994). Across-track distortion in the STAR-2 image precludes a good co-registration of the SAR and OPS data such was described earlier for the JERS-1 and ERS-1 SAR images in the Beaufort Sea, but a visual comparison of the two data types suggests that the regions of lowest albedo within the multiyear floe in the VNIR image corresponds to the darker tones in the SAR. At the time of the SAR acquisition, melt ponds were frozen, typically with a very smooth and bubble-free surface and a resulting low backscatter in the X band SAR image. The apparent patterns of melt pond coverage in the SAR and VNIR images suggest a floe made up of ice of different ages - perhaps with older multiyear ice embedded in a matrix of younger multiyear ice, in turn surrounded by first-year ice. In fact, differences in surface topography were noted in field observations, but not with precise enough locations for direct comparison with the imagery. Detailed surveys of a similar multiyear floe during the SIMMS 1993 experiment showed a clear distinction in hummock and meltpond

distributions at different portions of the 1993 floe.

2.1.4 Relative Albedo on First-year and Multiyear Ice

As noted above, melt ponds are likely to be warmer and shallower on smooth first-year ice, and deeper and more confined on multiyear ice. Physical models of the ice cover typically treat albedos independent of ice type, although melt ponds may have a substantial effect on equilibrium annual ice thicknesses (Ebert and Curry, 1993). Here, we consider the differences in albedo between first-year and multiyear ice by estimating "relative" narrow-band albedos using the OPS VNIR channel 1. Since the OPS data have not yet been calibrated, mean DN were estimated for open water and the brightest features in the image. A typical nadir-view albedo of 0.06 was assigned to open water (mean DN of 30) and an approximate albedo of 0.70 for melting snow (mean DN of 150). Assuming a linear relationship between albedo and DN as defined by these tie points, albedos were then estimated for DN averaged over the field-site multiyear floe (DN = 122, albedo = 0.65), average DN for drifting first-year ice floes in Figure 7 (DN = 94, albedo = 0.50) and for individual pixels of apparent bare-ice/melt pond area on the first-year floes (DN = 67, albedo = 0.36). While these albedos are only approximate, they demonstrate that large albedo differences are possible between ice types during peak summer melt.

2.2 Summary of OPS Retrievals of Sea Ice Conditions

The high spatial and spectral resolution of JERS-1 OPS imagery reveals details in surface features useful for mapping ice type, apparent melt pond fraction, and albedo as a function of ice type. Shape and texture differences are distinct enough to identify the multiyear ice floe studied during the spring field program in 1992. Surface features on the floe are consistent with melt pond coverage based on field observations prior to melt. The changes in ice conditions from late June to mid-July suggest that melt proceeded rapidly following the delayed onset of melt due to below-normal temperatures earlier in the summer. Approximate albedos indicate that the albedo of melting ice can vary substantially as a function of ice type.

3. Conclusions

The L band SAR and high-resolution OPS on board JERS-1 compliment other available spaceborne sensors for mapping sea ice conditions. In particular, combination of C band ERS-1 and L band JERS-1 SAR improves the discrimination of ice type compared to using either SAR image individually, and the high spatial and spectral resolution of the JERS-1 VNIR permit albedos to be mapped for individual-ice types. Such combinations should be a key element of programs such as the planned Surface Heat and Energy Balance (SHEBA) experiment that seek to understand how sea ice processes are represented at different scales.

Acknowledgements This work was supported by the NASA Polar Oceans Program, with data provided by the NASDA JERS-1 verification program and the ESA PIPOR program. Thanks are also due to the Alaska SAR Facility and the National Snow and Ice Data Center for providing data, NSERC and the Polar Continental Shelf Project for field support, and to the other members of the SIMMS field crew.

References

Barry, R.G., 1989. The present climate of the Arctic Ocean and possible past and future states, in *The Arctic Seas. Climatology, Oceanography, Geology, and Biology*, Y. Herman (ed), pp. 1-46, V. Nostrand Reinhold, NY.

Ebert, E.E. and J.A. Curry, 1993. An intermediate one-dimensional thermodynamic sea ice model for investigating ice-atmosphere interactions. *Journal of Geophysical Research*, 98(C6), 10,085-10,109.

Kwok, R., and G. Cunningham, 1993, Geophysical Processor System Data User's Handbook, Rep. D-9526, 91 pp., Jet Propulsion Laboratory, Pasadena, California.

Hallikainen, M., and D. P. Winebrenner, 1992, The physical basis for sea ice remote sensing, in *Microwave Remote Sensing of Sea Ice*, Frank Carsey (ed.), Geophysical Monograph 68, American Geophysical Union, 29-46.

Onstott, R. G., 1992, SAR and scatterometer signatures of sea ice, in *Microwave Remote Sensing of Sea Ice*, Frank Carsey (ed.), Geophysical Monograph 68, American Geophysical Union, 73-104.

Papakyriakou, T, 1992. Section 5.3, Surface climatology in, Reddan, S.P., D.G. Barber, and E.F. LeDrew, 1992. The SIMMS'92 Data Report. Earth Observations Laboratory Technical Report ISTS-EOL-SIMMS-TR-92-003, 226 pp.

Reddan, 1992. Section 2, Location, site descriptions, and snow and ice conditions, in, Reddan, S.P., D.G. Barber, and E.F. LeDrew, 1992. The SIMMS'92 Data Report. Earth Observations Laboratory Technical Report ISTS-EOL-SIMMS-TR-92-003, 226 pp.

Steffen, K. and J. Heinrichs, 1994, Feasibility of sea ice typing with synthetic aperture radar: Merging of Landsat Thematic Mapper and ERS-1 SAR imagery, *Journal of Geophysical Research*, 99(C11).

Winebrenner, D.P., E.D. Nelson, and R. Colony, 1994. Observations of melt onset on multiyear Arctic sea ice using the ERS 1 synthetic aperture radar. *Journal of Geophysical Research*, 99(C11), 22,425-22,441.

Table 1. Backscatter means and standard deviations for three sea ice types (Multiyear, First-year I, and First-year II) in data from the JERS-1 and ERS-1 SAR sensors.

	Number of points	ERS-1 backscatter (dB) Mean	St. Dev.	JERS-1 backscatter (dB) Mean	St. Dev.
Multiyear Ice	11653	-10.50	3.34	-17.06	4.55
First-year I	8067	-13.32	2.86	-13.91	4.18
First-year II	3231	-14.96	2.80	-13.05	4.03

Captions for Figures

Figure 1. Portion of an ERS-1 SAR image taken February 18, 1993 of an area in the Beaufort Sea at 76.3° N, 142.75° W. Nominal spatial resolution of the image is 12.5 m and the area covered is approximately 1.1 km square.

Figure 2. Portion of an JERS-1 SAR image concurrent with Figure 1.

Figure 3. Graphical representation of the image statistics listed in Table 1. Ellipses are centered on the mean backscatter values and have sizes corresponding to one standard deviation above and below the mean.

Figure 4. Color composite of coregistered JERS-1 (red) and ERS-1 SAR (green) images. Blue is not used in this composite.

Figure 5. AVHRR channel 1 image (June 27, 1992) showing the extent of ice cover in the central Canadian Archipelago. The coverage of the JERS-1 VNIR image used here is indicated by the white box.

Figure 6. Color composite of VNIR data for the SIMMS study region (red = channel 3, green = channel 2, blue = channel 1, and subsampled to a 90 m pixel size). Portions of Cornwallis and Devon islands appear at the western (left) and northeastern (top right) edges of the image in red tones, open water in black, and sea ice in shades of blue. The location of multiyear ice floe studied during the 1992 SIMMS field program and shown in Figure 8 is indicated by the box in Wellington Channel. Multiyear ice floes are interspersed with first-year ice within Wellington Channel, while the ice in Lancaster Sound is first-year ice.

Figure 7. Full-resolution VNIR composite subsection showing the fine detail visible in the drifting first-year ice floes within Lancaster Sound.

Figure 8. VNIR channel 3 (0.76-0.86 μm) subsection covering the SIMMS multiyear ice floe. Note the differences in mottling and gray tones attributed to surface melt on different ice types and for different portions of the floe.

Figure 9. STAR-2 SAR image of the same floe, acquired prior to melt. Smooth first-year ice surrounds the multiyear floe. The darker tones (lower backscatter) within the floe correspond to the areas of distinct mottling in the VNIR image.

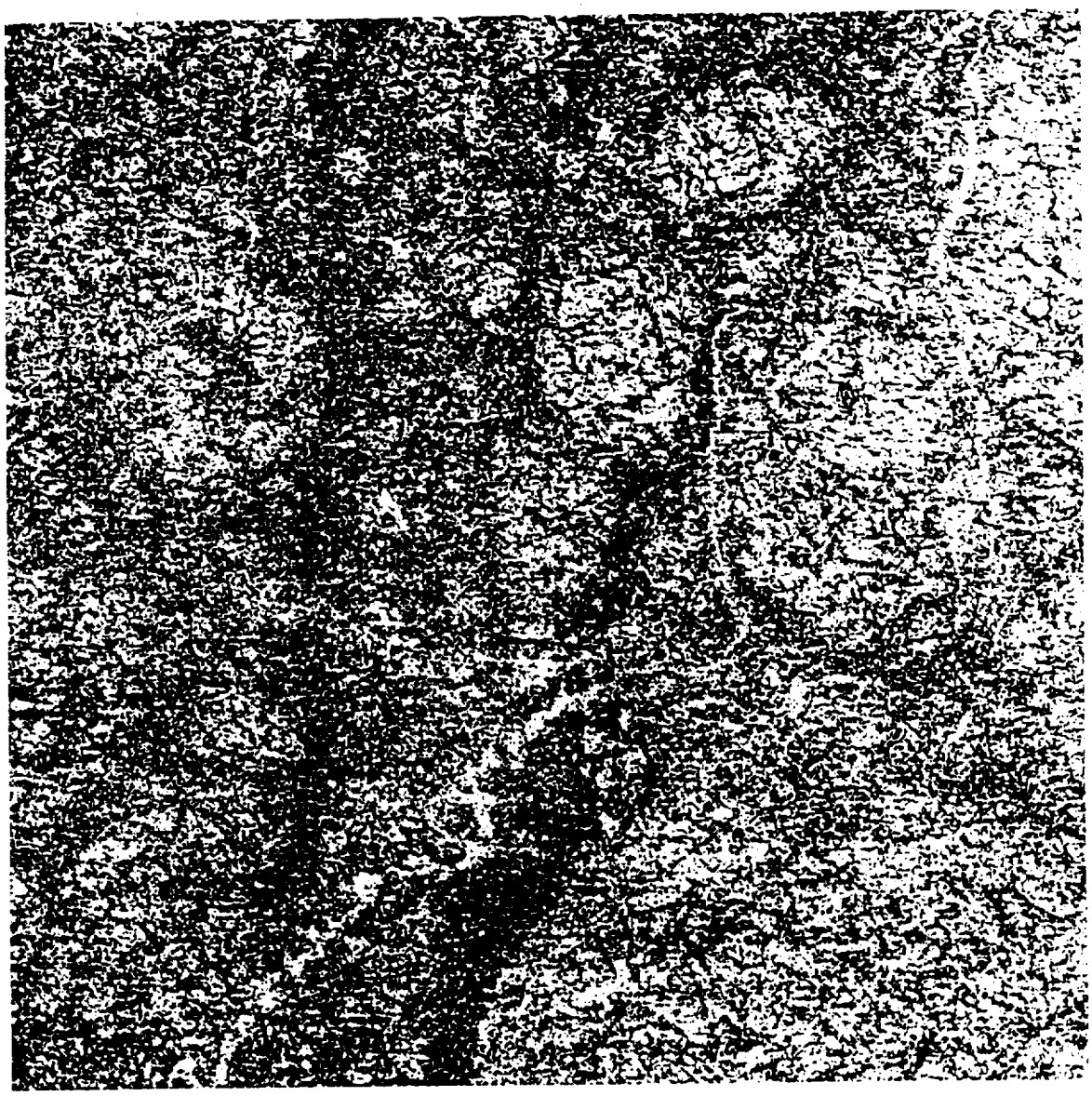

Fig 1

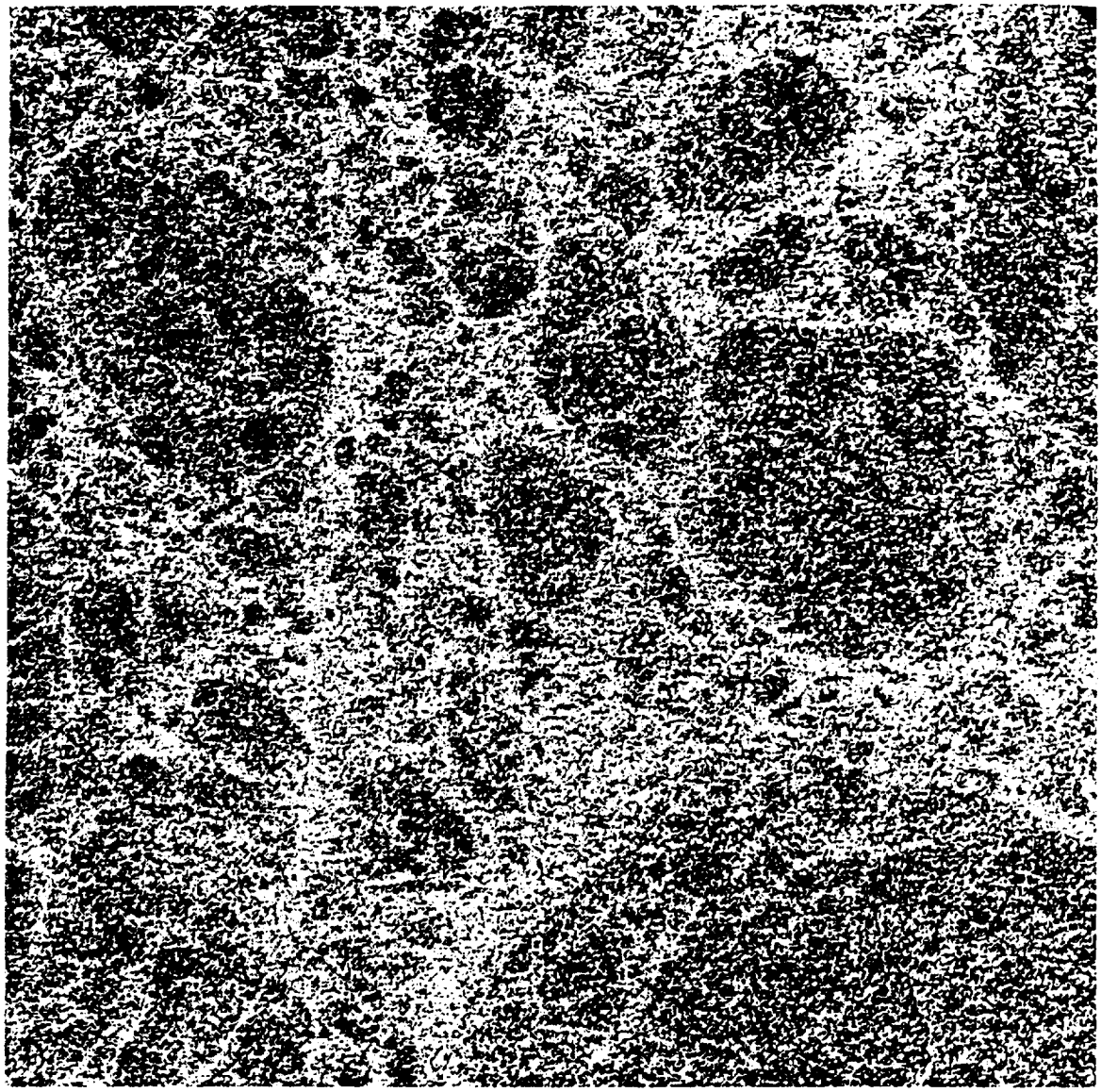

Fig 2

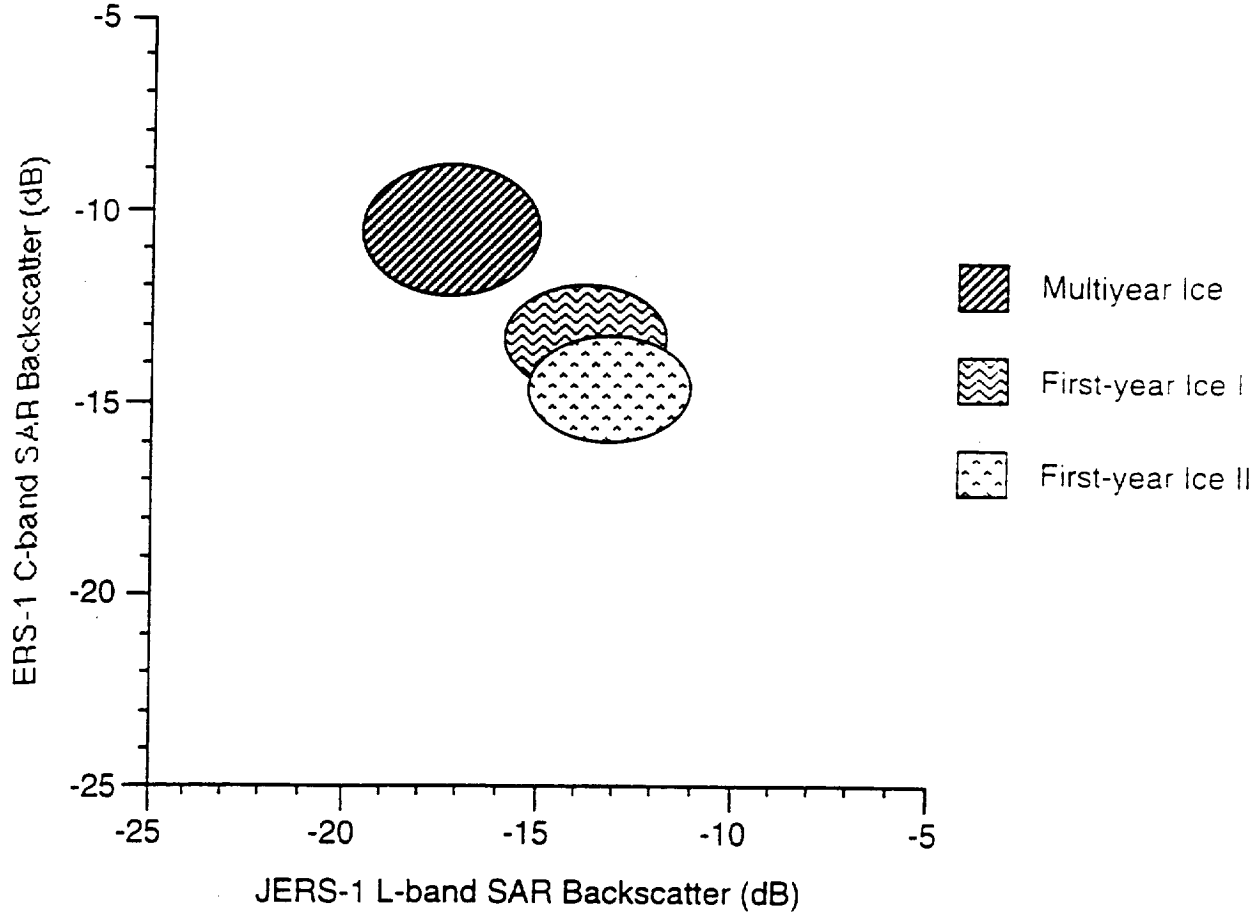
-5
-10
-15
-20
-25
ERS-1 C-band SAR Backscatter (dB)
-25
-20
-15
-10
-5
JERS-1 L-band SAR Backscatter (dB)
Multiyear Ice
First-year Ice I
First-year Ice II

Fig 3

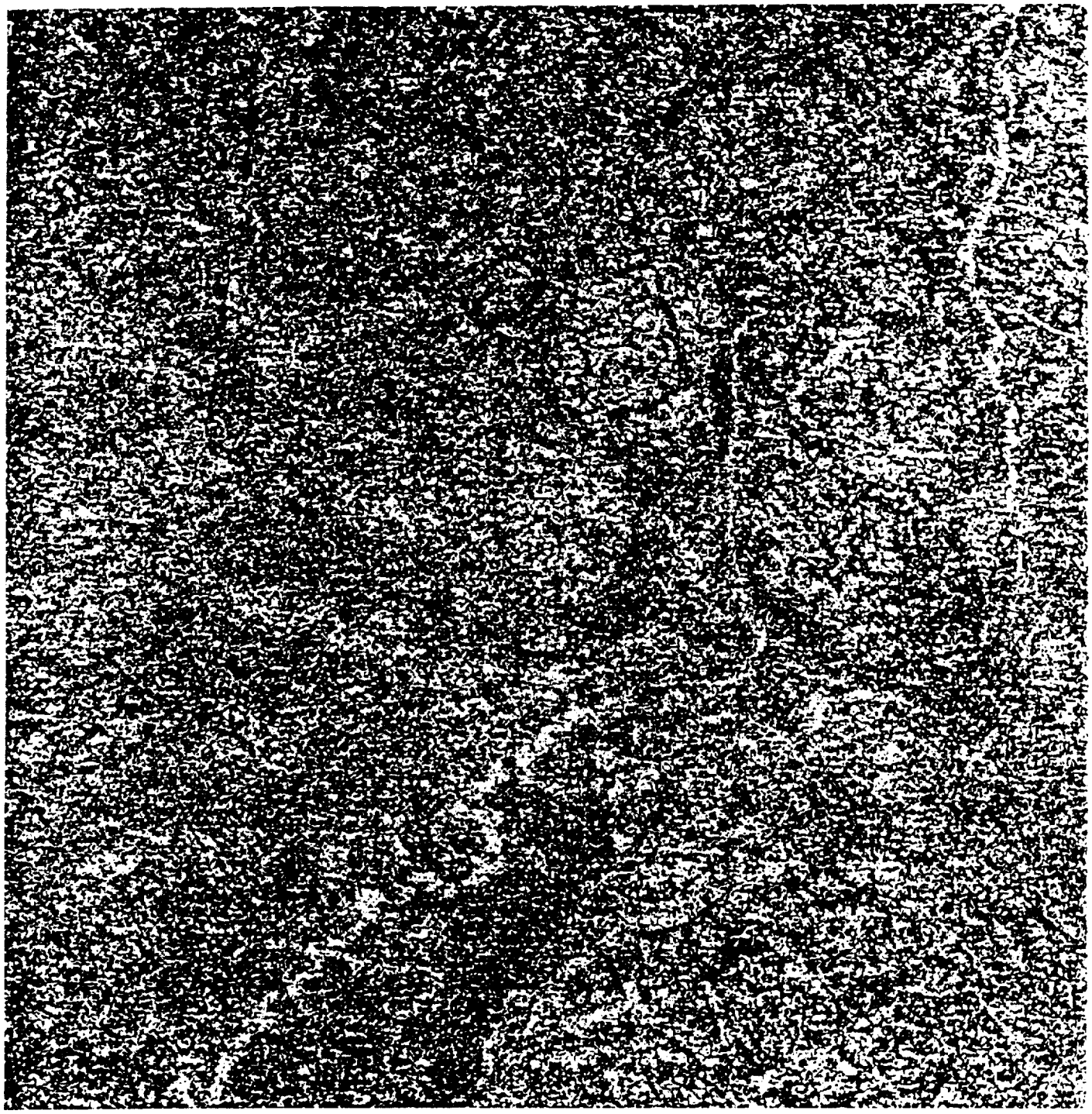

Fig 4

Fig 5

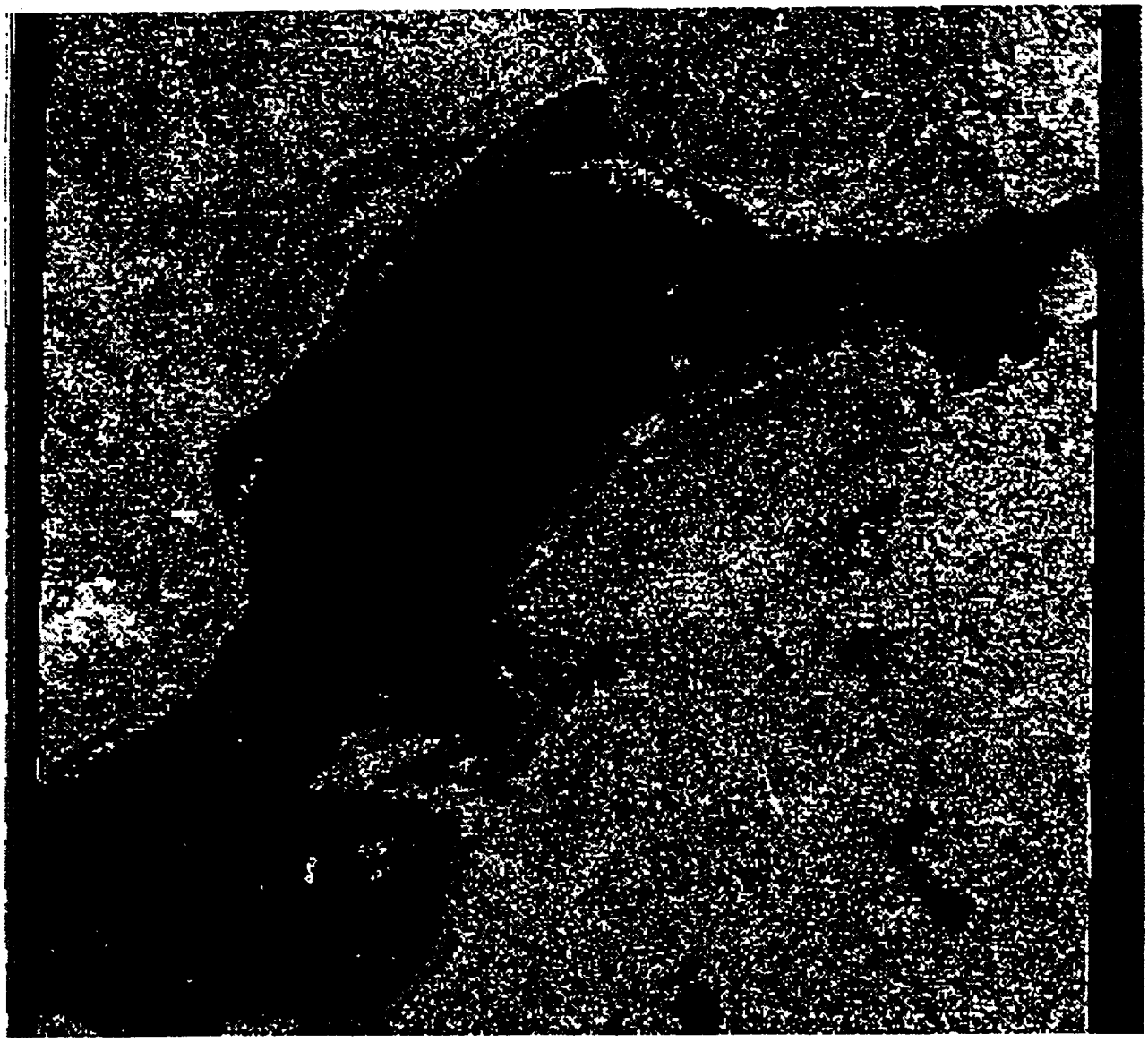

Fig 6

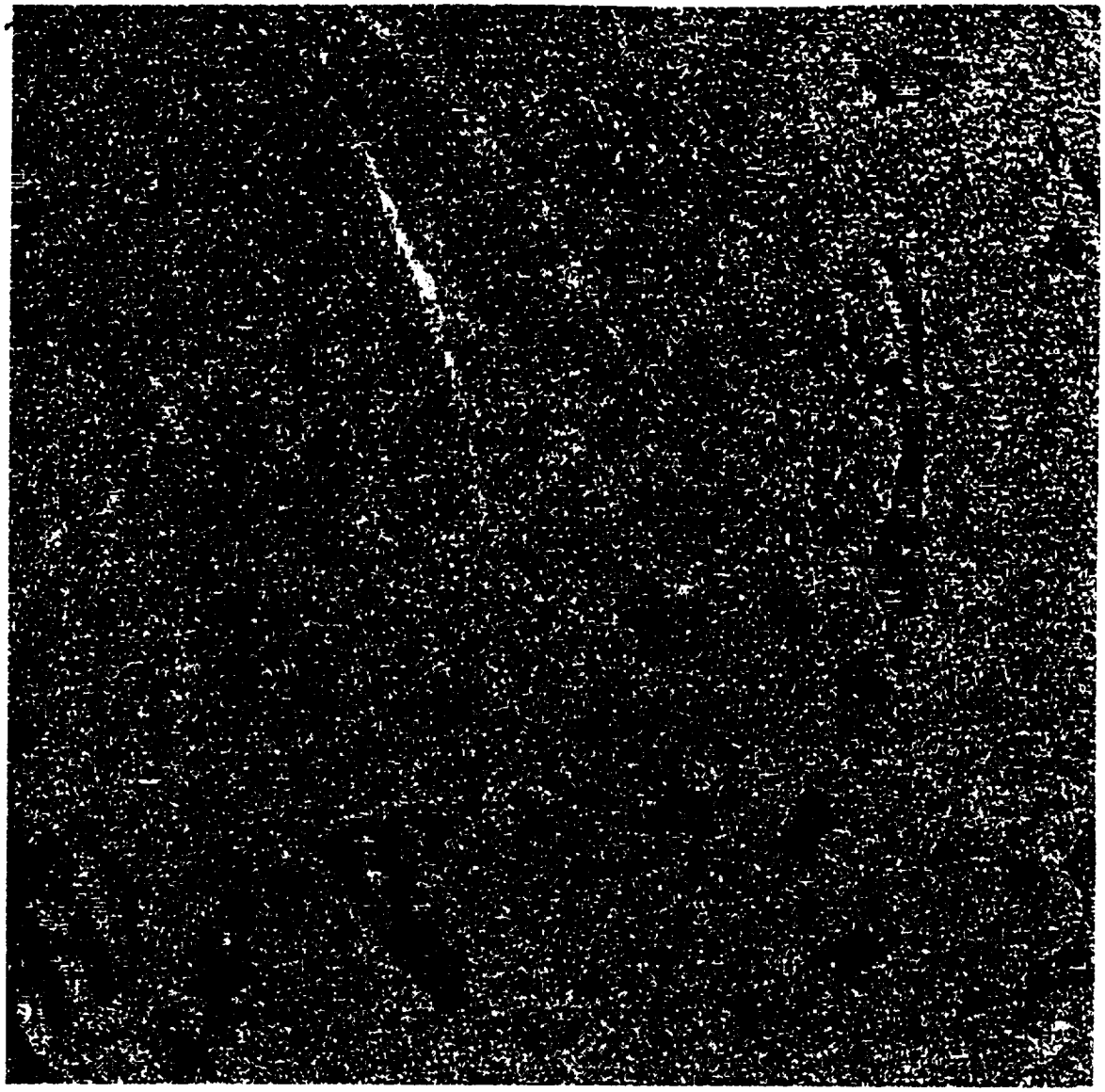

Fig 7

Fig 8

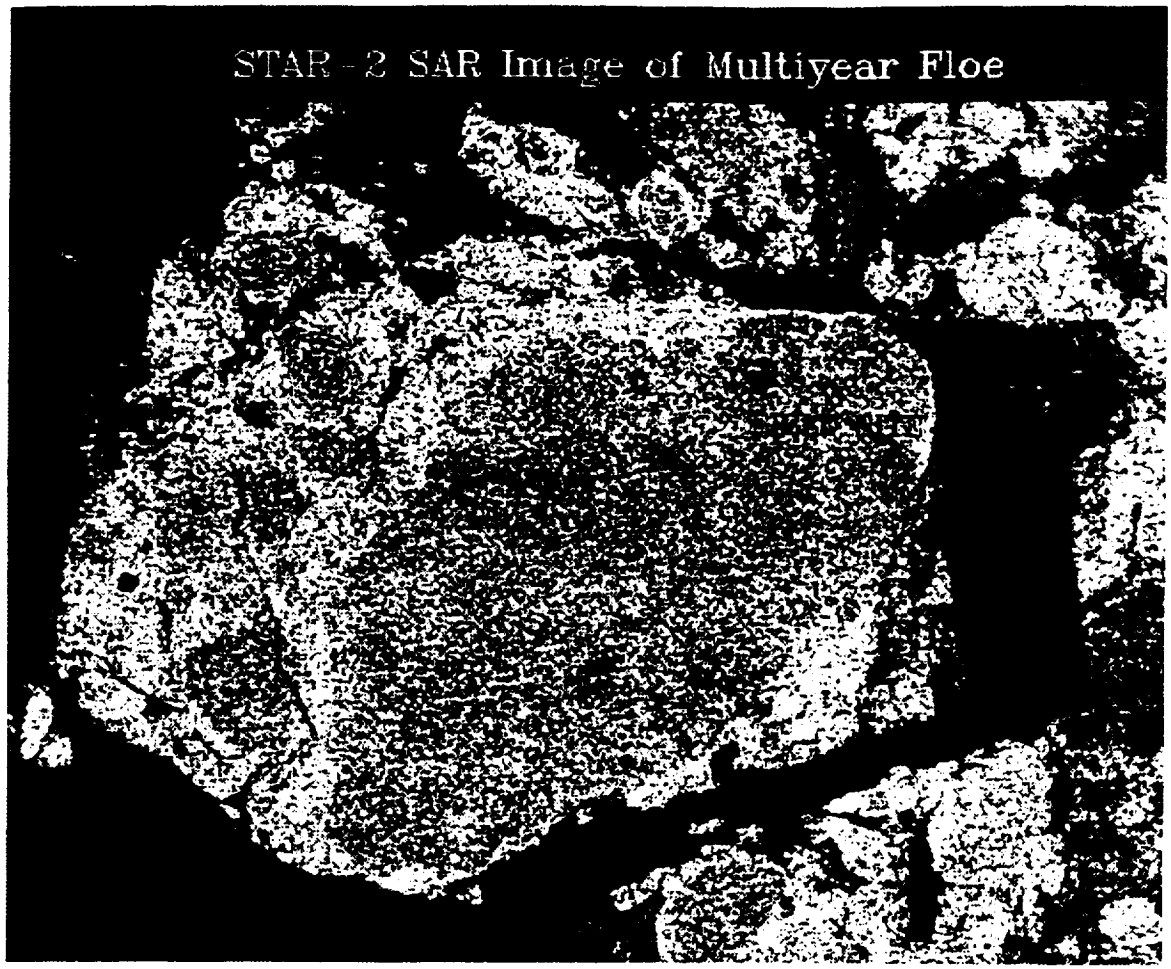

Fig 9